Distribution of Surface Wave Breaking Fronts

Leonel Romero[*]

Key Points:

- A new wave breaking model suitable for coupled models provides a framework to explicitly account for wave breaking related air-sea fluxes.
- The spectral wave breaking crest distributions model is consistent with field observations over a wide range of conditions.
- Wave breaking variability due to wave-current interactions is dominated by sub-mesoscale current variability.

[*]Earth Research Institute, University of California, Santa Barbara, CA 93106

Corresponding author: Leonel Romero, `leromero@eri.ucsb.edu`

Abstract

This study describes a model of Phillips' $\Lambda(\boldsymbol{c})$ distribution, which is the expected length of breaking fronts (per unit surface area) moving with velocity $\boldsymbol{c}$ to $\boldsymbol{c} + d\boldsymbol{c}$, providing a framework for coupled atmosphere-wave-ocean models to explicitly account for wave breaking related air-sea fluxes. The model of Λ depends on the spectral saturation, based on the statistics of the lengths of crest exceeding wave slope criteria, including long-wave short-wave modulation. A wave breaking dissipation function based on Λ was implemented in the model WaveWatchIII. The wave solutions are consistent with the observations, including several metrics of the spectrum and $\Lambda(c)$ distributions. The whitecap coverage derived from Λ reproduces recent parameterizations saturating at high winds. The wave breaking variability due to wave-current interaction is significant at submesoscales (order 1 km or smaller). The wave breaking model can be further developed to model gas transfer coefficients and aerosol production.

Plain Language Summary

This study introduces a new model of wave breaking that allows coupled atmosphere-wave-ocean models to explicitly account for wave breaking related air-sea exchanges, as well as direct applications for climate, weather, remote sensing, and biogeochemical studies. The model is based on a physical framework that allows explicit computations of wave breaking related air-sea fluxes including momentum, energy, gases, and aerosols across the air-sea interface. The energy dissipation from the new breaking model was implemented in a spectral wave model. The resulting wave model solutions accurately reproduce the main features of empirical wave energy spectra. The wave breaking distributions, and whitecap coverage from the model are consistent with field observations over a wide range of conditions. The results show that wave breaking variability is significantly modulated due to current variations at small scales.

1 Introduction

Surface wave breaking modulates the fluxes of energy, momentum, mass, and gases across the air-sea interface (W. Melville, 1996; Perlin et al., 2013). Breaking waves drive upper ocean currents and mixing (Phillips, 1977), affect aerosol production, and enhance gas exchange and heat fluxes across the air-sea interface (Thorpe, 1982; Farmer et al., 1993), all of which have implications for weather and

climate change predictions (Loewen, 2002). Air-sea fluxes have been traditionally parameterized with crude models based on wind speed. Phillips (1985) introduced a rational framework to describe the wave breaking kinematics and dynamics through a distribution $\Lambda(\boldsymbol{c})$, which is the expected length of breaking crests moving with velocity $\boldsymbol{c}$ to d$\boldsymbol{c}$ per unit surface area, with corresponding azimuth integrated distribution $\Lambda(c) = \int \Lambda(\boldsymbol{c})c\,d\theta$. The moments of $\Lambda(c)$ are related to the following physical parameters:

$$\text{Total length of breaking fronts per unit surface area: } L = \int \Lambda(\boldsymbol{c})d\boldsymbol{c} \tag{1}$$

$$\text{Fraction of total surface area turned over per unit time: } R = \int c\,\Lambda(\boldsymbol{c})d\boldsymbol{c} \tag{2}$$

$$\text{Fractional whitecap coverage: } W \propto \int c^2\,\Lambda(\boldsymbol{c})d\boldsymbol{c} \tag{3}$$

$$\text{Rate of air entrainment per unit surface area: } V_a \propto \int c^3\,\Lambda(\boldsymbol{c})d\boldsymbol{c} \tag{4}$$

$$\text{Momentum flux per unit surface area: } M \propto \int c^4\,\Lambda(\boldsymbol{c})d\boldsymbol{c} \tag{5}$$

$$\text{Energy dissipation per unit surface area: } E \propto \int c^5\,\Lambda(\boldsymbol{c})d\boldsymbol{c}, \tag{6}$$

for details the reader may refer to Phillips (1985), Kleiss and Melville (2010), and Deike et al. (2017).

Several studies have measured Λ using visible and/or infrared imaging techniques under various environmental conditions (Gemmrich et al., 2008; Thomson et al., 2009; Kleiss & Melville, 2010; Zappa et al., 2012; Schwendeman et al., 2014). The High-Resolution Air-Sea Interaction Experiment (HiRes) experiment provided measurements of $\Lambda(c)$ from visible imagery over areas with strong wave-current interactions (Romero et al., 2017), as well as coincident measurements of $\Lambda(c)$ from visible and infrared imagery over a wide range of wave ages (Sutherland & Melville, 2013, hereafter referred to as SM13). The infrared imagery of SM13 allowed quantification of wave breaking statistics for both waves that entrain air and micro-breakers. One of the main findings by SM13 was an empirical scaling of $\Lambda(c)$ approximately collapsing the data along a line proportional to c^{-6}.

There are, however, several shortcomings related to Phillips' framework as discussed by Zappa et al. (2016) and Banner et al. (2014). For example, it is not immediately obvious how to relate the speed of a breaking front to a particular scale. Although laboratory measurements suggest it is proportional to the phase speed (Rapp & Melville, 1990; Stansell & MacFarlane, 2002; Banner & Peirson, 2007),

the speed of a breaker slows down during the breaking process. Alternatively, other approaches have been proposed directly relating the energy dissipation to the bubble plume volume or the whitecap coverage (Hwang & Sletten, 2008; A. H. Callaghan, 2018).

Despite the controversy surrounding Phillips' framework, the findings by SM13 provide a benchmark for the development of a new model of $\Lambda(c)$ suitable for spectral wave models, and in particular for coupled atmosphere-wave-ocean models explicitly accounting for air-sea exchanges due to surface wave breaking. This study describes a new model of Λ, including its implementation and validation within the spectral model WaveWatch III (The WAVEWATCH III Development Group [WW3DG], 2016), here defined as WW3. The wave breaking model builds from the work by Romero and Melville (2011) on the length of crest exceeding wave slope thresholds. The model of $\Lambda(c)$ and its implementation in WW3 are described in Section 2. The model results are presented in Section 3, which are discussed and summarized in Sections 4 and 5, respectively.

2 Methods

2.1 Wave Breaking Model

The directional wavenumber spectrum $F(\boldsymbol{k})$ of surface waves is defined such that

$$\langle \eta^2 \rangle \;\; = \;\; \int F(\boldsymbol{k}) d\boldsymbol{k}, \tag{7}$$

with $\langle \eta^2 \rangle$ corresponding to the variance of the surface elevation. The azimuth integrated or omnidirectional spectrum is given by

$$\phi(k) = \int F(k, \theta) k \, d\theta. \tag{8}$$

The spectral evolution of the directional wave spectrum $F(\boldsymbol{k})$ in deep water can be described through the wave action conservation equation

$$\frac{\partial N(\boldsymbol{k})}{\partial t} + (\boldsymbol{c}_g + \boldsymbol{u}) \cdot \frac{\partial N(\boldsymbol{k})}{\partial \boldsymbol{x}} - \boldsymbol{k} \cdot \frac{\partial \boldsymbol{u}}{\partial \boldsymbol{x}} \frac{\partial N}{\partial \boldsymbol{k}} = \frac{S_{in} + S_{nl} + S_{ds}}{\sigma}, \tag{9}$$

where $N(\boldsymbol{k}) = F(\boldsymbol{k})/\sigma(k)$ is the wave action, $\sigma(\boldsymbol{k}) = (gk)^{1/2}$ is the frequency according to the linear dispersion relationship, $\boldsymbol{u}$ is the surface current, and S is the sum of the energy sources (K. Hasselmann et al., 1973). The dominant energy source terms

101 are composed of wind input S_{in}, nonlinear four-wave resonant fluxes S_{nl}, dissipation

102 due to wave breaking S_{ds}.

103 In this study, the wind input S_{in} is modeled according to Ardhuin et al. (2010)

104 based on the quasilinear theory by Janssen (1991), including short-wave sheltering

105 due to longer waves (Chen & Belcher, 2000) and swell dissipation for waves traveling

106 faster than the wind, using the default tuning parameters of the ST4 package with a

107 maximum roughness length Z0MAX= 8×10^{-4}. Thus limiting the drag coefficient

108 to 1.85×10^{-3} (Sullivan et al., 2012). The nonlinear energy fluxes are computed with

109 the standard Direct Interaction Approximation (DIA - S. Hasselmann and Hassel-

110 mann 1985) and the âĂIJexactâĂİ Webb-Resio-Tracy method (WRT -Tracy and

111 Resio 1982, van Vledder 2006).

112 The spectral dissipation S_{ds} is computed through $\Lambda(\boldsymbol{k})$, which is modeled on

113 the assumption that it is proportional to the statistics of crest lengths exceeding a

114 wave slope criterion. Following the work by Longuet-Higgins (1957), Romero and

115 Melville (2011) derived an analytical model describing the statistical distribution of

116 the length of crests per unit surface area and unit bandwidth for waves exceeding

117 wave slope criterion s_o according to

$$l_{s_o} = \frac{1}{3} \frac{s_o}{2 m_{00}^{1/2} \bar{k}} \exp\left(-\frac{s_o^2}{2 m_{00} \bar{k}^2}\right), \tag{10}$$

119 where $m_{00} = \langle \eta^2 \rangle$, and $\bar{k}$ is the mean wavenumber. Romero and Melville (2011)

120 showed good agreement between equation (10) and bandpassed airborne lidar wave

121 observations (Romero & Melville, 2010a, hereafter referred to as RM10). Assum-

122 ing that wave groups are self-similar and a functional form as in equation (10) with

123 respect to the spectral saturation $B(\boldsymbol{k}) = F(\boldsymbol{k})k^4$, $\Lambda(\boldsymbol{k})$ is modeled according to

$$\Lambda(\boldsymbol{k}) = \frac{l}{k} \exp\left(-\frac{B_{br}}{B(\boldsymbol{k})}\right) M_L(\boldsymbol{k}) M_W(k), \tag{11}$$

125 where B_{br} is a characteristic saturation representative of the breaking waves, l is a

126 dimensionless function, $M_L(\boldsymbol{k})$ is a function accounting for the breaking modulation

127 by the longer waves, and $M_W(k)$ is an amplification for the short waves to balance

128 the wind input. The spectral saturation is a convenient parameter to characterize

129 the wave slope locally within a broadband spectrum assuming self-similarity and

130 has been shown to correlate with breaking waves in the field (Banner et al., 2002)

131 and used extensively to model wave breaking (Donelan, 2001; Alves & Banner, 2003;

132 Ardhuin et al., 2010; Banner & Morison, 2010).

133   Donelan (2001) proposed a nonlinear spectral dissipation function due to wave

134   breaking that accounts for the straining of the short waves by the longer waves

135   in terms of the cumulative mean-squared slope cmss(k). Following Peureux et al.

136   (2018) and Guimaraes (2018), the wave breaking modulation due to longer waves is

137   modeled according to

$$M_L(\boldsymbol{k}) = \left(1 + 400\sqrt{\text{cmss}(k)}\cos^2(\theta - \theta_w)\right)^{3/2}, \tag{12}$$

139   where the cumulative mean-squared slope

$$\text{cmss}(k) = \int_0^k F(k,\theta) k^2 \, dk \, d\theta, \tag{13}$$

141   and θ_w is the spectrally weighted mean wave direction defined as

$$\theta_w = \tan\left(\frac{\int F(\boldsymbol{k})\sin\theta \, d\boldsymbol{k}}{\int F(\boldsymbol{k})\cos\theta \, d\boldsymbol{k}}\right). \tag{14}$$

143   The factor of 400 and the power of 3/2 in equation (12) were found to give the best

144   performance against the measurements by RM10 with respect to the bimodal direc-

145   tional distribution at wavenumbers larger than the spectral peak.

146   The wind modulation function is modeled linearly according to

$$M_W(k) = (1 + D\max[1, \frac{k}{k_o}])/(1 + D) \tag{15}$$

148   with $k_o(u_*) = g\left(\frac{3}{28u_*}\right)^2$. Therefore $M_W(k)$ is only activated for $k > k_o$ balancing

149   the wind input while maintaining a saturation level at large wavenumbers consistent

150   with the field observations (i.e., RM10 and Lenain and Melville 2017). The dimen-

151   sionless factor $D = 0.9$ for the DIA and $D = 2$ for WRT computations. The larger

152   value of D and a wider range of resolved wavenumbers are need for WRT computa-

153   tions to minimize the variability of the spectral saturation at large wavenumbers.

154   By definition, the total length of breaking crests per unit surface area

$$L = \int \Lambda(\boldsymbol{k}) d\boldsymbol{k} \tag{16}$$

156   and

$$\Lambda(\boldsymbol{c})d\boldsymbol{c} = \Lambda(\boldsymbol{k})d\boldsymbol{k}. \tag{17}$$

158   Following Phillips (1985), an element of area $d\boldsymbol{k}$ corresponds to an area element $d\boldsymbol{c}$

159   as given by

$$
\begin{aligned}
d\boldsymbol{k} &= k \, dk \, d\theta \tag{18}\\
&= -\frac{\partial k}{\partial c}\frac{k}{c} c \, dc \, d\theta, \tag{19}
\end{aligned}
$$

which according to the linear dispersion relationship $c = (g/k)^{1/2}$ becomes

$$dk = -\frac{2g^2}{c^6} c \, dc \, d\theta \tag{20}$$

$$= -\frac{2g^2}{c^6} dc \tag{21}$$

and

$$\Lambda(\boldsymbol{c}) = -\frac{2g^2}{c^6} \Lambda(\boldsymbol{k})\Big|_{k=gc^{-2}}, \tag{22}$$

which integrated in azimuth becomes

$$\Lambda(c) = -\frac{2g}{c^3} \Lambda(k)\Big|_{k=gc^{-2}}. \tag{23}$$

Laboratory measurements have shown that the speed of breaking crests (c_{br}) is linearly related to the phase speed through a factor α, such that $c_{br} = \alpha c$, with α varying between 0.7 and 0.95 (Rapp & Melville, 1990; Stansell & MacFarlane, 2002; Banner & Peirson, 2007). For consistency with SM13, here it is assumed that $\alpha = 1$.

Duncan (1981, 1983) introduced a scaling of the energy dissipation rate per unit length of breaking crest according to

$$\epsilon_l = \frac{b\rho_w c^5}{g}, \tag{24}$$

where b is a dimensionless parameter representing the strength of breaking. Laboratory measurements have shown that b depends on the wave steepness and the rate of energy convergence of wave groups varying between 1×10^{-4} and 1×10^{-1} (W. K. Melville, 1994; Banner & Peirson, 2007; Drazen et al., 2008). Phillips (1985) generalized equation (24) for a broadband spectrum according to

$$\rho_w \, g \, S_{ds}(\boldsymbol{c}) d\boldsymbol{c} = \frac{\rho_w}{g} \, b \, \Lambda(\boldsymbol{c}) c^5 d\boldsymbol{c}, \tag{25}$$

such that

$$S_{ds}(\boldsymbol{c}) = \frac{b}{g^2} \, \Lambda(\boldsymbol{c}) c^5 \text{ or } S_{ds}(\boldsymbol{k}) = \frac{b}{g^2} \, \Lambda(\boldsymbol{k}) c^5. \tag{26}$$

Subsequently, Romero et al. (2012) combined a semi-empirical quantification of the spectral energy dissipation with measurements of $\Lambda(c)$ by Kleiss and Melville (2010) to show that the strength of breaking b is not a constant across the spectrum. They proposed the model

$$b(k) = A(B(k)^{1/2} - B_T^{1/2})^{5/2}, \tag{27}$$

where $B(k) = \phi(k)k^3$ is the azimuth integrated saturation, A is a dimensionless factor of order unity, and B_T is a breaking saturation threshold (Banner et al., 2002),

and the power of 5/2 is based on the inertial scaling by Drazen et al. (2008). Here I use $A= 3.8$ and $B_T = 1.1 \times 10^{-3}$, which are within the range of values obtained by Romero et al. (2012).

The spectral dissipation due wave breaking $S_{ds}(\boldsymbol{k})$ is modeled combining equations (11-15), (26) and (27). The dissipation written solely in terms of either wavenumber or frequency is included for clarity in the supplemental material. The constants l and B_{br} were tuned under idealized duration-limited runs such that the significant wave height (H_s) and peak wave period (T_p) matched Ardhuin et al. (2010) (ST4), and the equilibrium range level matched Resio et al. (2004). The resulting coefficients are $B_{br} = 5 \times 10^{-3}$ and $l = 3.5 \times 10^{-5}$ for solutions forced with either DIA or WRT. The wave breaking saturation parameter B_{br} controls the shape of the spectrum at the peak and/or intermediate wavenumbers. As B_{br} increases, the spectral peakedness and the level of the equilibrium range decrease and vice versa.

After implementation of the $\Lambda(\boldsymbol{k})$ based dissipation, two additional output parameters were implemented in WW3: the whitecap coverage and air entraining rate. Following Kleiss and Melville (2010), the whitecap coverage is modeled according to

$$W = \frac{2\pi}{g} \gamma \int c^2 \, \Lambda(\boldsymbol{c}) d\boldsymbol{c}, \tag{28}$$

where γ is a dimensionless factor representing the duration of breaking relative to the wave period ($2\pi c/g$). Here γ is set to 0.56 and the lower limit of integration $c = 2$ m/s (Deike et al., 2017). Deike et al. (2017) developed a model for the rate of entrained air volume per unit area of ocean surface (V_a) based on direct numerical simulations (DNS). The model was further developed for field conditions in terms of $\Lambda(c)$ according to

$$V_a = \frac{\chi A}{g} \int (B^{1/2}(k) - B_T^{1/2})^{3/2} c^3 \, \Lambda(\boldsymbol{c}) d\boldsymbol{c}, \tag{29}$$

where A is the proportionality factor of the strength of breaking (27), and χ is a constant representing the ratio between the work done by buoyancy forces and mechanical dissipation, here set to $\chi = 0.2$. Again the lower limit of integral (29) is set to 2 m/s. Deike and Melville (2018) subsequently extended the model of air entrainment rate to model the bubble-mediated gas transfer coefficient of CO_2, which can be easily adapted in WW3.

2.2 Duration-Limited Experiments

Following Romero (2008), duration-limited experiments were conducted with stationary winds for model tuning and validation. The model runs consist of the source-term integration test case of WW3 (ww3_ts1). The spectrum was discretized with a resolution $\Delta\theta = 10^o$ in azimuth and $\Delta k/k = 0.14$ in wavenumber. The lowest wavenumber resolved is 0.0016 rad/m and the upper is 4 and 10 rad/m for the DIA and WRT, respectively. A larger upper value is needed with "exact" computations of the nonlinear energy fluxes to minimize the variability of the degree of saturation at large wavenumbers. The global time step was set to 300 s and the minimum dynamical the source term integration step was set to 15 s. All model computations in this study allow the tail of the spectrum to evolve freely without a prognostic tail (Lui et al. 2009).

The model was integrated for 12 days starting with "calm" conditions ($H_s = 0$) with the linear wind input source term enabled (Cavaleri & Malanotte-Rizzoli, 1981). Duration-limited solutions were generated for wind speeds between 4 and 35 m/s, saving output every 20 minutes. The model was tuned against ST4 solutions of H_s and T_p with normalized root-mean-square errors (NRMSE, equation 26 of Ardhuin et al. 2010) of less than 5% for winds speeds between 4 and 35 m/s.

2.3 Regional Model Configuration

There is a growing interest within the community to better understand the modulation of the wave field, including wave breaking, due to wave-current interactions (Zippel & Thomson, 2017; Ardhuin et al., 2017; Romero et al., 2017). Here, the wave breaking variability due to wave-current interactions is investigated with a regional model configuration forced with surface currents from a High-Frequency radar array with a horizontal resolution of 2 km (Kaplan & Largier, 2006; Kaplan et al., 2005). The model solutions are validated against lidar wave observations collected from an aircraft (Romero et al., 2017). The domain 81x64 grid points in space with a resolution of 0.01^o (1 km). The bathymetry consists of the 1 km product SRTM30_PLUS from Becker et al. (2009). The time steps were set to 20 seconds with the minimum dynamical source term integration of 5 seconds. The spectral grid has an azimuthal resolution of 10° and $\Delta k/k = 0.2$ with wavenumbers between

253 0.0016 and 4 rad/m. The initial and boundary conditions were generated using

254 the measured directional wavenumber spectra (Romero et al., 2017) extrapolated

255 from 0.4 to 4 rad/m following Romero et al. (2012). Boundary conditions were kept

256 constant but the forcing winds and currents varied in time. Time-varying forcing

257 surface winds were provided homogeneously using the field measurements from FLIP

258 (Grare et al., 2013) with a temporal resolution of 30 minutes. For comparison, an

259 additional model run was forced with relative winds (i.e., $\boldsymbol{U}_{10} - \boldsymbol{u}(\boldsymbol{x})$, where $\boldsymbol{u}(\boldsymbol{x})$

260 corresponds to the surface current).

261 **3 Results**

262 **3.1 Wave Spectrum**

263 In this section, the wave model performance is analyzed with an idealized solu-

264 tion forced with 20 m/s winds. Omnidirectional spectra at various wave ages c_p/u_*

265 are shown in Figure 1a, comparing DIA and WRT computations. The solutions

266 show the typical differences with narrower spectra for the "exact" nonlinear en-

267 ergy fluxes (S. Hasselmann & Hasselmann, 1985). The shape of the omnidirectional

268 spectra above the spectral peak approximately follows two power-law regimes: an

269 equilibrium range $\phi \sim k^{-5/2}$ followed by a saturation range $\phi \sim k^{-3}$, in agreement

270 with the measurements (Long & Resio, 2007; Romero & Melville, 2010a; Lenain &

271 Melville, 2017). This is better shown with $B(k) = \phi(k)k^3$ in Figure 1b. The energy

272 level within the equilibrium range is slightly larger for the DIA solutions. Following

273 Toba (1973), the equilibrium range can be scaled according to

$$\phi(k) = \frac{\beta}{2} u_* g^{-1/2} k^{-5/2}, \tag{30}$$

275 where β is a dimensionless factor with weak dependence on the wave age c_p/u_*

276 (Resio et al. 2004, RM10). Following Liu et al. (2019), β is calculated from model

277 solutions for $2.25\,k_p < k < 0.35$ rad/m, with 0.35 rad/m corresponding to the upper

278 limit before the noise-floor of the data collected by RM10. The mean compensated

279 spectrum is calculated according to

$$\langle \phi k^{5/2} \rangle = \frac{1}{0.35 - 2.25k_p} \int_{2.25k_p}^{0.35} \phi(k)k^{5/2} dk, \tag{31}$$

281 and

$$\beta = \frac{2g^{1/2}}{u_*} \langle \phi k^{5/2} \rangle. \tag{32}$$

283   Figure 1c shows β vs wave age from DIA and WRT solutions compared against the

284   measurements by Resio et al. (2004) and RM10. The model solutions are in good

285   agreement against Resio et al. (2004), roughly 20% larger than RM10. At large

286   wavenumbers, the saturation level approximately reaches that reported by Lenain

287   and Melville (2017) of 7×10^{-3} and RM10 of $7.3 \pm 1.0 \times 10^{-3}$.

288   The wave solutions are further characterized with respect the directional

289   spreading calculated according to

$$\sigma_\theta = \frac{\int_{-\pi/2}^{\pi/2} F(k,\theta)|\theta|d\theta}{\int_{-\pi/2}^{\pi/2} F(k,\theta)d\theta}, \tag{33}$$

291   limiting the integral to $\pm\pi/2$ for consistency with the RM10 lidar data which has a

292   180° ambiguity. The spreading $\sigma_\theta(k/k_p)$ is shown in Figures 1d,e for the DIA and

293   WRT solutions, respectively, in good agreement against RM10 (shown in Figure 1f).

294   Overall, the WRT solution gives better spreading against RM10, approaching the

295   spreading reported by Hwang et al. (2000) for fully developed seas. This is a sub-

296   stantial improvement compared to other WRT solutions which tend to give much

297   narrower spectra (Romero & Melville, 2010b; Liu et al., 2019).

3.2 Wave Breaking Distributions

299   In this section, the $\Lambda(c)$ distributions from duration-limited solutions are com-

300   pared against SM13 in Figures 2a,b. The comparison is not one-to-one because the

301   observed Λ's include very old waves reaching values of $c_p/u_* = 100+$, which sug-

302   gests a mixture of wind-sea and swell. Nevertheless, the agreement between the

303   model and observations is reasonable. The model solutions are further analyzed with

304   the empirical scaling proposed by SM13, specifically $\Lambda' = \Lambda(c)c_p^2 g^{-1}\sqrt{c_p/u_*}$ and

305    $c' = c/\sqrt{gH_s}(gH_s/c_p^2)^{0.1}$. Figure 2c,d, shows both sets of $\Lambda(c)$ scaled accordingly,

306   collapsing along $0.05\,c'^{-6}$.

3.3 Whitecap Coverage and Air Entrainment

308   The computed whitecap coverage W over a wide range of winds speeds (4 m/s

309    $\leq U_{10} < 35$ m/s) from duration limited solutions is shown in Figure 3a. The results

310   compare well with the parameterizations by Schwendeman and Thomson (2015),

311   A. Callaghan et al. (2008), and Brumer et al. (2017). The model solutions exhibit

312 a saturating trend for large wind speeds consistent with the observations, within

313 the scatter of the data by Holthuijsen et al. (2012). The saturation of Λ and its mo-

314 ments comes from its dependence on $\exp(-B_{br}/B(\boldsymbol{k}))$, which tends to saturate as

315 the equilibrium range level increases with increasing wind speed.

316 The rate of entrained air volume per unit surface area V_a normalized by peak

317 wave speed c_p is plotted in Figure 3b as a function of the friction velocity u_* nor-

318 malized by the ballistic velocity $\sqrt{gHs}$ for winds between 4 and 16 m/s. The data

319 are plotted over the values obtained by Deike et al. (2017) based on field measure-

320 ments of $\Lambda(c)$. The model results show good agreement with Deike et al. (2017).

321 The air entrainment rate computations within WW3 can be easily extended to

322 model the bubble-mediated gas transfer of CO_2 based on the work by Deike and

323 Melville (2018).

3.4 Wave-current interactions

325 The wave breaking variability due to wave-current interactions is investi-

326 gated with the regional model configuration in Northern California as described

327 Section 2.3. Romero et al. (2017) collected novel field observations of directional

328 wavenumber spectra and wave breaking statistics across the edge of an upwelling

329 jet, which overlapped with a narrow area with enhanced wave breaking along a sub-

330 mesoscale front. Here I focus on the wave breaking solutions across the upwelling

331 jet/submesoscale front. A snapshot of the model whitecap coverage is plotted to

332 compare the field observations in Figure 4a. The modeled whitecap coverage is

333 qualitatively consistent along the flight track across the jet/front, with significant

334 differences towards the northeastern part of the sampling region. The location of

335 the submesoscale front is shown with a thick black line at the edge of the jet. The

336 observed whitecap coverage exhibits considerably larger spatial variability than the

337 model solutions likely in part due to statistical sampling and submesoscale current

338 variability not resolved by the HF radar. The model solutions of $\Lambda(c)$ on either

339 side of the submesoscale front along the flight track crossing the front are shown

340 in Figure 4b in qualitative agreement against the field observations for $c\quad > 3$ m/s.

341 At lower speeds, the observed $\Lambda(c)$ distributions from visible imagery roll-off much

342 faster. The $\Lambda(c)$ distributions are larger on the colder side of the front primarily due

343 to direct forcing and straining of the waves by the currents across the upwelling jet.

344 The effect of relative winds against spatially homogeneous winds is small, which can

345 be seen by comparing the thick and thin red and blue lines in Figure 4b.

4 Discussion

347   The results demonstrate that the new dissipation model based on Λ gives

348 excellent wave model performance with spectra characterized by two power-law

349 regimes (equilibrium and saturation) consistent with empirical data, and directional

350 spreading consistent with that reported by RM10. Moreover, the directional dis-

351 tribution of the spectrum above the spectral peak is bimodal with lobe separations

352 consistent with RM10. The bimodality is mainly due to the modulation transfer

353 function which dissipates more energy in the direction of the longer dominant waves,

354 which favors the non-linear energy fluxes (Peureux et al., 2018). This has impor-

355 tant implications for directionality of the mean-squared-slope and the prediction of

356 microseisms (Munk, 2009) and will be explored elsewhere.

357   An advantage of a dissipation model based on Λ is that it can be directly

358 used to calculate the various wave breaking related parameters and air-sea fluxes,

359 including the effects of wave-current interactions. The test case presented with

360 wave-current interactions based on relatively coarse HF radar currents gave reduced

361 spatial variability of breaking compared to the observations. This is further explored

362 here with a wave model configuration with 100 m resolution, forced with currents

363 from the Regional Ocean Modeling System (ROMS - Shchepetkin and McWilliams

364 2009), and the Weather Research and Forecasting Model (WRF). Figure 5a shows a

365 snapshot of simulated whitecap coverage (W) off the central coast of California with

366 substantial variability due to wave-current interactions. Figure 5b shows a zoom

367 over an area with enhanced wave breaking qualitatively similar to the photograph

368 in Romero et al. 2017 (Figure 1). The "line" of increased wave breaking overlaps

369 with a submesoscale front with strong horizontal shear, surface convergence, and

370 strong downwelling (Figures 5c,d). These effects are consistent with Rascle et al.

371 (2017) who showed that the mean-squared-slope is enhanced along fronts in con-

372 ditions with winds blowing obliquely to the front due to increased wave straining

373 downwind by the current gradients. Similarly, the line of enhanced wave breaking

374 in Romero et al. (2017) occurred in conditions with winds obliquely aligned with a

375 submesoscale front. As discussed by Romero et al. (2017) enhanced wave breaking

376　over submesoscale fronts with strong surface convergence and downwelling velocities

377　have potentially important implications for gas transfer. This and a wide range of

378　phenomena due to wave-breaking modulated air-sea fluxes including feedbacks can

379　be investigated with a coupled atmospheric-wave-ocean model within the framework

380　of this study.

381　　　　Finally as discussed earlier, this study assumes that the observed speeds of

382　the breaking waves (c_{br}) corresponds to the linear phase speed (c). But laboratory

383　measurements suggest that $c_{br} = \alpha c$, with α between 0.7 and 0.95. This implies that

384　the observed $\Lambda(c_{br})$ when converted to $\Lambda(c)$ becomes

$$\Lambda(c) = \Lambda(c_{br})\Big|_{\alpha c} \frac{\partial c_{br}}{\partial c}. \tag{34}$$

386　Then assuming that $\Lambda(c_{br}) \sim c_{br}^{-6}$ as approximately supported by the observations,

387　equation (34) would give $\Lambda(c) \sim \alpha^{-5}c^{-6}$. In that case, in order to maintain the same

388　level of dissipation within the model while matching the observed Λ with $\alpha \neq 1$,

389　the parameters l and A would have to be adjusted accordingly with compensating

390　factors α^{-5} and α^5, respectively. This would increase $\Lambda(c)$ by a factor between 6 and

391　1.3 and reduce b by a factor between 0.16 and 0.77 for values of $\alpha = 0.7$ and 0.95,

392　respectively. However, this level of uncertainty is well within the uncertainty of the

393　empirical scaling of Λ' (Figure 2d), and also within the scatter of the observed vari-

394　ability of the strength of breaking from laboratory experiments (Romero et al., 2012;

395　Wang & Wijesekera, 2018). It is expected that the uncertainties will become smaller

396　in the future as more measurements become available and new techniques are devel-

397　oped. The interested reader may refer to the supplemental material for additional

398　plots that show the spectral strength of breaking and its effective value against field

399　measurements by Zappa et al. (2016) and references within. Other plots show the

400　azimuth-integrated dissipation $S_{ds}(k)$, and the product $b(c)\Lambda(c)$ comparing favorably

401　with expected power-laws within the equilibrium range according to Phillips (1985).

5 Conclusions

403　　　　This study describes a model of Λ suitable for coupled atmosphere-wave-ocean

404　models. The wave breaking model depends on the spectral saturation and is based

405　on Gaussian statistics of the lengths of crests exceeding wave slope criteria. The

406　breaking modulation due to long-wave short-wave interaction is incorporated nonlin-

early through the cumulative mean-squared-slope. Direct modulation by the wind is included at large wave-numbers to match the wind input and ensure a saturation level consistent with the observations. A wave breaking dissipation based on Λ was implemented in WW3 within the source term package by Ardhuin et al. (2010). The wave model performance is excellent, producing spectra with approximately two-power law regimes, an equilibrium range ($\phi \sim k^{-5/2}$) followed by a saturation range ($\phi \sim k^{-3}$). The wave model gives directional spreading rates very similar to those reported by RM10, including solutions forced by the "exact" nonlinear resonant interactions which typically result in much narrower spectra (Romero & Melville, 2010b).

The $\Lambda(c)$ model is consistent with the field observations by SM13. The derived whitecap agrees with recent empirical parameterizations for wind speeds between 4 and 35 m/s, saturating at higher winds. The modeled rate of air entraining agrees with the calculations by Deike et al. (2017) from measurements of $\Lambda(c)$. Wave break-ing variability due to wave-current interactions were investigated with currents mea-sured by HF radar. The results are qualitatively consistent with the measurements by Romero et al. (2017), but the measurements exhibit substantially more vari-ability at small scales, likely due to statistical sampling and submesoscale current variability not resolved by the HF radar.

Acknowledgments

References

Alves, J.-H. G., & Banner, M. L.   (2003).   Performance of a saturation-based

dissipation-rate source term in modeling the fetch-limited evolution of wind waves. *J. Phys. Ocean.*, *33*, 1274–1298.

Ardhuin, F., Rogers, E., Babanin, A. V., Filipot, J.-F., Magne, R., Roland, A., . . . Collard, F. (2010, sep). Semiempirical Dissipation Source Functions for Ocean Waves. Part I: Definition, Calibration, and Validation. *J. Phys. Ocean.*, *40*(9), 1917–1941.

Ardhuin, F., Suzuki, N., Mcwilliams, J. C., & Aiki, H. (2017). Comments on âĂŸA Combined Derivation of the Integrated and Vertically Resolved, Coupled WaveâĂŞCurrent Equations. *J. Phys. Ocean.*, *47*(9), 2377–2385.

Banner, M. L., Gemmrich, J. R., & Farmer, D. M. (2002). Multiscale measurements of ocean wave breaking probability. *Journal of physical oceanography*, *32*, 3364–3375.

Banner, M. L., & Morison, R. P. (2010, jan). Refined source terms in wind wave models with explicit wave breaking prediction. Part I: Model framework and validation against field data. *Ocean Model.*, *33*(1-2), 177–189.

Banner, M. L., & Peirson, W. L. (2007, aug). Wave breaking onset and strength for two-dimensional deep-water wave groups. *J. Fluid Mech.*, *585*, 93.

Banner, M. L., Zappa, C. J., & Gemmrich, J. R. (2014). A Note on the Phillips Spectral Framework for Ocean Whitecaps*. *J. Phys. Ocean.*, *44*(7), 1727–1734.

Becker, J. J., Sandwell, D. T., Smith, W. H. F., & Braud, J. (2009). Global Bathymetry and Elevation Data at 30 Arc Seconds Resolution : SRTM30 _ PLUS. *Marine Geodesy*, *32*, 355–371.

Brumer, S. E., Zappa, C. J., Brooks, I. M., Tamura, H., Brown, S. M., Blomquist, B. W., . . . Cifuentes-Lorenzen, A. (2017). Whitecap Coverage Dependence on Wind and Wave Statistics as Observed during SO GasEx and HiWinGS. *J. Phys. Ocean.*, *47*(9), 2211–2235.

Callaghan, A., De Leeuw, G., Cohen, L., & O'Dowd, C. D. (2008). Relationship of oceanic whitecap coverage to wind speed and wind history. *Geophys. Res. Lett.*, *35*(23), 1–5.

Callaghan, A. H. (2018). On the Relationship between the Energy Dissipation Rate of Surface-Breaking Waves and Oceanic Whitecap Coverage. *J. Phys. Ocean.*, *48*(11), 2609–2626.

Cavaleri, L., & Malanotte-Rizzoli, P. (1981). Wind-wave prediction in shallow water. *J. Geophys. Res.*, *86*, 10,961–10,973.

Chen, G., & Belcher, S. E. (2000). Effects of long waves on wind-generated waves. *J. Phys. Ocean.*, *30*, 2246–2256.

Deike, L., Lenain, L., & Melville, W. K. (2017). Air entrainment by breaking waves. *Geophys. Res. Lett.*, *44*(8), 3779–3787.

Deike, L., & Melville, W. K. (2018, oct). Gas Transfer by Breaking Waves. *Geophys. Res. Lett.*, *45*(19), 10,482–10,492.

Donelan, M. A. (2001). A nonlinear dissipation function due to wave breaking. In *Proceedings of ecmwf workshop on ocean wave forecasting, 2âĂŞ4 july* (pp. pages 87– 94).

Drazen, D. A., Melville, W. K., & Lenain, L. (2008, aug). Inertial scaling of dissipation in unsteady breaking waves. *J. Fluid Mech.*, *611*, 307–332.

Duncan, J. H. (1981). An experimental investigation of breaking waves produced by a towed hydrofoil. *Proceedings of the Royal Society of London. Series A*, *377*(1770), 331–348.

Duncan, J. H. (1983). The breaking and non-breaking wave resistance of a two-dimensional hydrofoil. *J. Fluid Mech.*, *126*, 507–520.

Farmer, D. M., McNeil, C. L., & Johnson, B. D. (1993). Evidence for the importance of bubbles in increasing air-sea gas flux. *Nature*, *361*, 620–623.

Gemmrich, J. R., Banner, M. L., & Garrett, C. (2008, jun). Spectrally Resolved Energy Dissipation Rate and Momentum Flux of Breaking Waves. *J. Phys. Ocean.*, *38*(6), 1296–1312.

Grare, L., Lenain, L., & Melville, W. K. (2013, oct). Wave-Coherent Airflow and Critical Layers over Ocean Waves. *J. Phys. Ocean.*, *43*(10), 2156–2172.

Guimaraes, P. V. (2018). *Sea surface and energy dissipation* (Unpublished doctoral dissertation). Université Bretagne Loire.

Hasselmann, K., Barnett, T. P., Bouws, E., Carlson, H., Cartwright, D. E., Enke, K., . . . Walden, H. (1973). *Measurements of wind-wave growth and swell decay during the Joint North Sea Wave Project (JONSWAP)* (Vol. 46; Tech. Rep.). Deutches Hydrographisches Institut.

Hasselmann, S., & Hasselmann, K. (1985). Computations and Parameterizations of the Nonlinear Energy Transfer in a Gravity-Wave Specturm. Part II: Parame-

504   terizations of the Nonlinear Energy Transfer for Application in Wave Models.

505   *J. Phys. Ocean.*, *15*, 1378–91.

506   Holthuijsen, L. H., Powell, M. D., & Pietrzak, J. D. (2012, sep). Wind and waves in

507   extreme hurricanes. *J. Geophys. Res.*, *117*(C9), 1–15.

508   Hwang, P. A., & Sletten, M. A. (2008). Energy dissipation of wind-generated waves

509   and whitecap coverage. *J. Geophys. Res.: Oceans*, *113*(2), 1–12.

510   Hwang, P. A., Wang, D. W., Walsh, E. J., Krabill, W. B., & Swift, R. N.   (2000).

511   Airborne Measurements of the Wavenumber Spectra of Ocean Surface Waves.

512   Part II: Directional Distribution*. *J. Phys. Ocean.*, *30*, 2768–2787.

513   Janssen, P. A. E. M. (1991). Quasi-linear Theory of Wind-Wave Generation Applied

514   to Wave Forecasting. *J. Phys. Ocean.*, *21*, 1631–1642.

515   Kaplan, D. M., & Largier, J. (2006, dec). HF radar-derived origin and destination of

516   surface waters off Bodega Bay, California. *Deep-Sea Res. Part II: Topical Stud-

517   ies in Oceanography*, *53*(25-26), 2906–2930.

518   Kaplan, D. M., Largier, J., & Botsford, L. W. (2005). HF radar observations of sur-

519   face circulation off Bodega Bay (northern California, USA).   *J. Geophys. Res.*,

520   *110*(C10020), 1–25.

521   Kleiss, J. M., & Melville, W. K. (2010). Observations of wave breaking kinematics in

522   fetch-limited seas. *J. Phys. Ocean.*, *40*, 2575–2604.

523   Lenain, L., & Melville, W. K.   (2017).   Measurements of the Directional Spectrum

524   across the Equilibrium Saturation Ranges of Wind-Generated Surface Waves.

525   *J. Phys. Ocean.*, *47*, 2123–2138.

526   Liu, Q., Rogers, W. E., Babanin, A. V., Young, I. R., Romero, L., Zieger, S., . . .

527   Guan, C.   (2019, feb).   Observation-Based Source Terms in the Third-

528   Generation Wave Model WAVEWATCH III: Updates and Verification.   *J.*

529   *Phys. Ocean.*, *49*(2), 489–517.

530   Loewen, M. (2002). Inside whitecaps. *Nature*, *418*, 830.

531   Long, C. E., & Resio, D. T.   (2007).   Wind wave spectral observations in Currituck

532   Sound, North Carolina. *J. Geophys. Res.: Oceans*, *112*(5), C05001.

533   Longuet-Higgins, M. S.   (1957).   The statistical analysis of a random, moving sur-

534   face.   *Philosophical Transactions of the Royal Society of London A*, *249*(966),

535   321–387.

536   Melville, W. (1996). The Role of Surface-Wave Breaking in Air-Sea Interaction. *An-*

nual Review of Fluid Mechanics, *28*(1), 279–321.

Melville, W. K. (1994). Energy Dissipation by Breaking Waves. *J. Phys. Ocean.*, *24*(10), 2041–2049.

Munk, W. (2009). An Inconvenient Sea Truth: Spread, Steepness, and Skewness of Surface Slopes. *Annual Review of Marine Science*, *1*(1), 377–415.

Perlin, M., Choi, W., & Tian, Z. (2013, jan). Breaking Waves in Deep and Intermediate Waters. *Annual Review of Fluid Mechanics*, *45*(1), 115–145.

Peureux, C., Veras-Guimaraes, P., & Ardhuin, F. (2018). A modulation source term for short ocean waves numerical modelling. In *Egu general assembly conference abstracts* (Vol. 20, p. 16494).

Phillips, O. M. (1977). *The Dynamics of the Upper Ocean* (Vol. 2nd). Cambridge University Press.

Phillips, O. M. (1985). Spectral and statistical properties of the equilibrium range in wind-generated gravity waves. *J. Fluid Mech.*, *156*, 505–531.

Rapp, R. J., & Melville, W. K. (1990). Laboratory Measurements of Deep-Water Breaking Waves. *Philosophical Transactions of the Royal Society of London A*, *331*(1622), 735–800.

Rascle, N., Molemaker, J., Marié, L., Nouguier, F., Chapron, B., Lund, B., & Mouche, A. (2017). Intense deformation field at oceanic front inferred from directional sea surface roughness observations. *Geophys. Res. Lett.*, *44*(11), 5599–5608.

Resio, D. T., Long, C. E., & Vincent, C. L. (2004). Equilibrium-range constant in wind-generated wave spectra. *J. Geophys. Res.*, *109*(C1), C01018.

Romero, L. (2008). *Airborne observations and numerical modeling of fetch-limited waves in the Gulf of Tehuantepec* (Unpublished doctoral dissertation). University of California, San Diego.

Romero, L., Lenain, L., & Melville, W. K. (2017). Observations of Surface-Wave-Current Interaction. *J. Phys. Ocean.*, *47*, 615–632.

Romero, L., & Melville, W. K. (2010a). Airborne Observations of Fetch-Limited Waves in the Gulf of Tehuantepec. *J. Phys. Ocean.*, *40*(3), 441–465.

Romero, L., & Melville, W. K. (2010b). Numerical Modeling of Fetch-Limited Waves in the Gulf of Tehuantepec. *J. Phys. Ocean.*, *40*(3), 466–468.

Romero, L., & Melville, W. K. (2011). Spatial Statistics of the Sea Surface in Fetch-

Limited Conditions. *J. Phys. Ocean.*, *41*(10), 1821–1841.

Romero, L., Melville, W. K., & Kleiss, J. M.   (2012, jan).   Spectral Energy Dissipation due to Surface-Wave Breaking. *J. Phys. Ocean.*, *42*, 1421–1444.

Schwendeman, M., & Thomson, J.   (2015, dec).   Observations of whitecap coverage and the relation to wind stress, wave slope, and turbulent dissipation.   *J. Geophys. Res.: Oceans*, *120*(12), 8346–8363.

Schwendeman, M., Thomson, J., & Gemmrich, J. R.   (2014, jan).   Wave Breaking Dissipation in a Young Wind Sea. *J. Phys. Ocean.*, *44*(1), 104–127.

Shchepetkin, A. F., & McWilliams, J. C.   (2009, dec).   Correction and commentary for âĂIJOcean forecasting in terrain-following coordinates: Formulation and skill assessment of the regional ocean modeling systemâĂİ by Haidvogel et al., J. Comp. Phys. 227, pp. 3595âĂŞ3624.   *Journal of Computational Physics*, *228*(24), 8985–9000.

Stansell, P., & MacFarlane, C.   (2002).   Experimental investigation of wave breaking criteria based on wave phase speeds. *J. Phys. Ocean.*, *32*, 1269–1283.

Sullivan, P. P., Romero, L., McWilliams, J. C., & Melville, W. K. (2012, nov). Transient Evolution of Langmuir Turbulence in Ocean Boundary Layers Driven by Hurricane Winds and Waves. *J. Phys. Ocean.*, *42*(11), 1959–1980.

Sutherland, P., & Melville, W. K.   (2013, jun).   Field measurements and scaling of ocean surface wave-breaking statistics.   *Geophys. Res. Lett.*, *40*(12), 3074–3079.

Sutherland, P., & Melville, W. K.   (2015, apr).   Field Measurements of Surface and Near-Surface Turbulence in the Presence of Breaking Waves.   *J. Phys. Ocean.*, *45*(4), 943–965.

The WAVEWATCH III Development Group [WW3DG].   (2016).   User manual and system documentation of WAVEWATCH III version 5.16. Tech. Note 329, NOAA/NWS/NCEP/MMAB, College Park, MD, USA.   *Technical note, MMAB Contribution*, *276*(329), 326 pp. + Appendices.

Thomson, J., Gemmrich, J. R., & Jessup, A. T.   (2009).   Energy dissipation and the spectral distribution of whitecaps. *Geophys. Res. Lett.*, *36*(11), 4–7.

Thorpe, S. A.   (1982).   On the clouds of bubbles formed by breaking wind-waves in deep water, and their role in air-sea gas transfer. *Philosophical Transactions of the Royal Society of London A*, *304*, 155–210.

Toba, Y. (1973). Local Balance in the Air-Sea Boundary Processes. III. *Journal of the Oceanographical Society of Japan*, *29*, 209–220.

Tracy, B., & Resio, D. T. (1982). *Theory and Calculation of the nonlinear energy transfer between sea waves in deep water* (Tech. Rep.). WIS Technical Report 11. US Army Engineer Waterways Experiment Station, Vicksburg, Mississippi, USA: Hydraulics Lab.

van Vledder, G. P. (2006, feb). The WRT method for the computation of non-linear four-wave interactions in discrete spectral wave models. *Coastal Engineering*, *53*(2-3), 223–242.

Wang, D. W., & Wijesekera, H. W. (2018). Observations of Breaking Waves and Energy Dissipation in Modulated Wave Groups. *J. Phys. Ocean.*, *48*(12), 2937–2948.

Zappa, C. J., Banner, M. L., Morison, R. P., & Brumer, S. E. (2016). On the Variation of the Effective Breaking Strength in Oceanic Sea States a . *J. Phys. Ocean.*, *46*(7), 2049–2061.

Zappa, C. J., Banner, M. L., Schultz, H., Gemmrich, J. R., Morison, R. P., Lebel, D. A., & Dickey, T. (2012). An overview of sea state conditions and air-sea fluxes during RaDyO. *J. Geophys. Res.: Oceans*, *117*(5), 1–23.

Zippel, S., & Thomson, J. (2017, apr). Surface wave breaking over sheared currents: Observations from the Mouth of the Columbia River. *J. Geophys. Res.: Oceans*, *122*(4), 3311–3328.

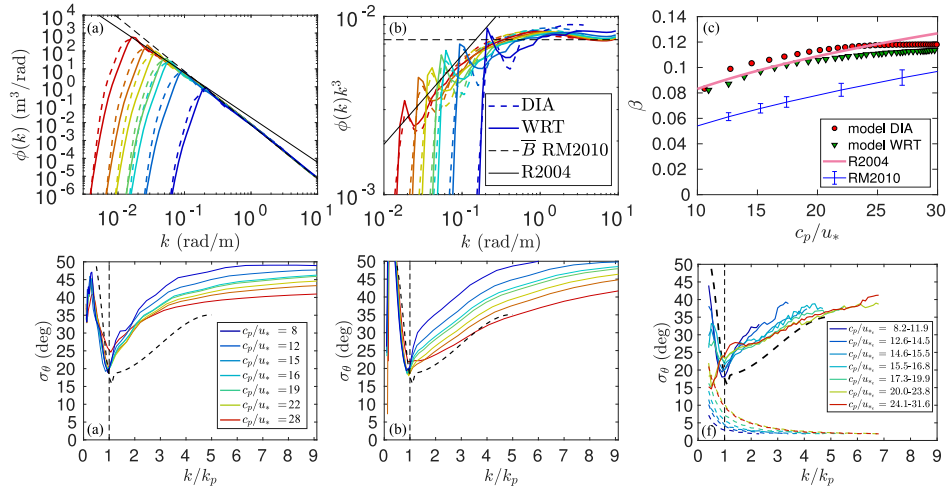**Figure 1.** Evolving omnidirectional spectra (a) and corresponding compensated (saturation) spectra $\phi\,k^3$ (b) color coded by wave age, with reference power-laws of $k^{-5/2}$ and k^{-3} shown with black solid and dashed lines, respectively. Toba's coefficient β is plotted against the wave age c_p/u_* in (c) and compared against Resio et al. (2004) and RM10. (d,e) Directional spreading $\sigma_\theta(k/k_p)$ from DIA and WRT solutions, respectively. (f) The directional spreading data from RM10 (solid lines), with dashed lines colored lines indicating the error magnitude. The black dahsed lines in (d-f), corresponds to the directional spreading from lidar observations by Hwang et al. (2000).
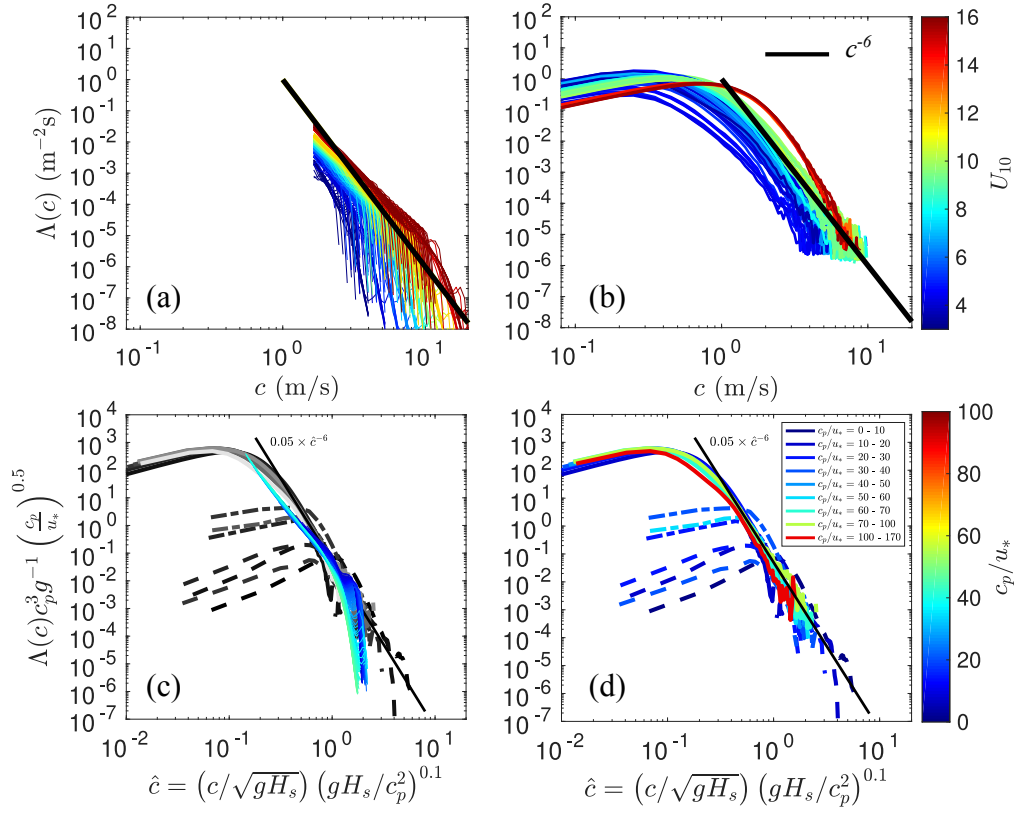
Figure 2. (a) $\Lambda(c)$ model solutions compared to SM13 (b), color coded by wind speed, with corresponding nondimensionalized distributions in (c) and (d), respectively. The black straight lines show reference power-laws of c^{-6}. The modeled nondimensionalized $\Lambda(c)$ distributions are in good agreement with the observations (gray colors), collapsing along the $0.05\ \hat{c}^{-6}$ line, within the scatter of the data.
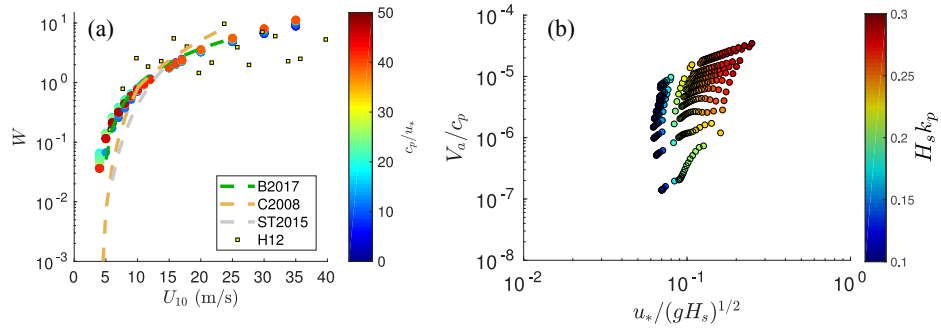
Figure 3. (a) Whitecap coverage solutions as a function of wind speed, color coded by wave age. The green, orange, gray dashed lines show the parameterizations by Brumer et al. (2017), A. Callaghan et al. (2008), and Schwendeman and Thomson (2015), respectively. The yellow squares correspond the data by Holthuijsen et al. (2012). (b) Rate of entrained air volume per unit area of ocean surface (V_a, small circles) normalized by the peak phase speed (c_p) as a function of friction velocity normalized by the ballistic velocity ($c_p/H_s)^{1/2}$. Data are plotted over the figure by (Deike et al., 2017), color coded by the significant slope criteria ($H_s k_p = H_s g/c_p^2$)
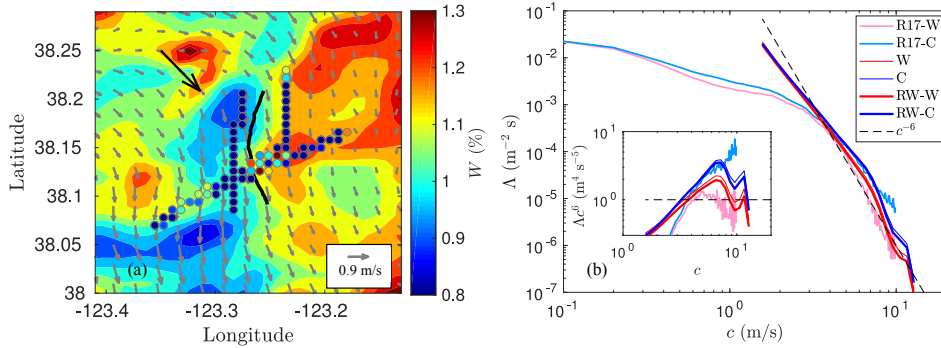

Figure 4. (a) Snapshot of modeled whitecap coverage W compared to the measurements by Romero et al. 2017 (circles). The gray arrows show the HF radar surface currents. The black arrow shows the wind direction and the thick black line indicates the location of the observed submesoscale front at the edge of the upwelling jet. (b) Model and observed $\Lambda(c)$ across the submesoscale front. The red (pink) and blue (light blue) lines correspond to model solutions (observations - R17) on the warm and cold sides of the front, respectively. The model solutions shown with thick lines where forced with homogeneous winds as opposed to those forced with relative winds (RW) shown with thick lines. For reference, see $\Lambda(c)$ sampling flight tracks in Romero 2107 (Fig. 7e).
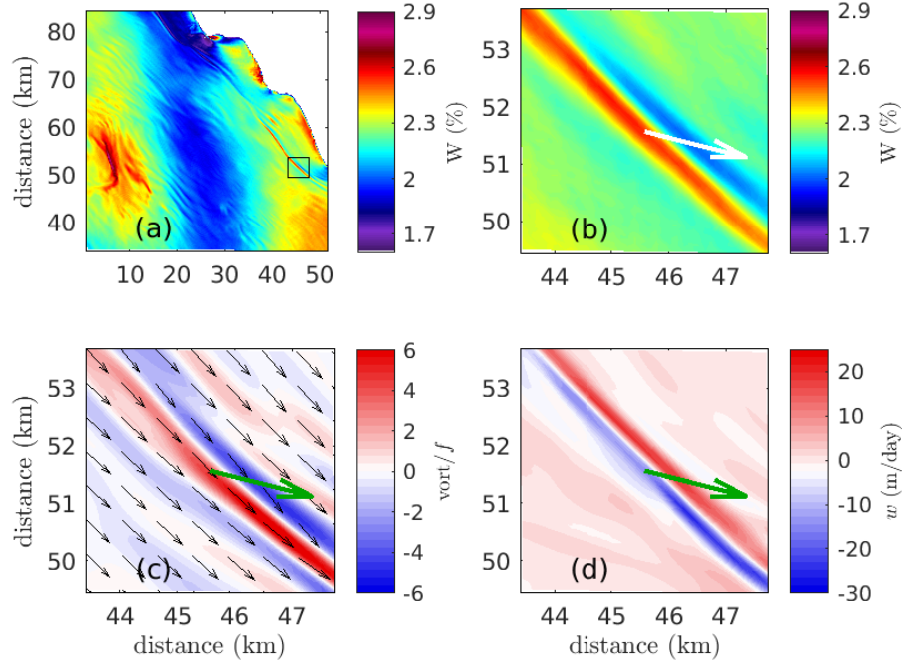
Figure 5. (a) Simulated whitecap coverage along the central coast of California. (b) Zoom over area with enhanced wave breaking, with corresponding vorticity normalized by the Coriolis parameter (c), and vertical velocity (d). The large arrow in (b-d) show the mean wind direction. The arrows in (c) show the surface currents.